PHYSICS OF FLUIDS **28**, 025106 (2016)

Direct numerical simulation of the flow around an aerofoil in ramp-up motion

Marco E. Rosti, Mohammad Omidyeganeh, and Alfredo Pinelli
School of Mathematics, Computer Science and Engineering, City University London, London EC1V 0HB, United Kingdom

(Received 24 December 2015; accepted 27 January 2016; published online 9 February 2016)

A detailed analysis of the flow around a NACA0020 aerofoil at $Re_c = 2 \times 10^4$ undergoing a ramp up motion has been carried out by means of direct numerical simulations. During the manoeuvre, the angle of attack is linearly varied in time between 0° and 20° with a constant rate of change of $\dot{\alpha}_{\mathrm{rad}} = 0.12 U_\infty / c$. When the angle of incidence has reached the final value, the lift experiences a first overshoot and then suddenly decreases towards the static stall asymptotic value. The transient instantaneous flow is dominated by the generation and detachment of the dynamic stall vortex, a large scale structure formed by the merging of smaller scales vortices generated by an instability originating at the trailing edge. New insights on the vorticity dynamics leading to the lift overshoot, lift crisis, and the damped oscillatory cycle that gradually matches the steady condition are discussed using a number of post-processing techniques. These include a detailed analysis of the flow ensemble average statistics and coherent structures identification carried out using the Q-criterion and the finite-time Lyapunov exponent technique. The results are compared with the one obtained in a companion simulation considering a static stall condition at the final angle of incidence $\alpha = 20°$. © *2016 AIP Publishing LLC.* [http://dx.doi.org/10.1063/1.4941529]

I. INTRODUCTION

Dynamic stall is an unsteady phenomenon that appears on lifting objects in response to time variations of the angle of attack. A classical example is the flow over aerofoils undergoing large amplitude pitching motions that can lead to dramatic changes in the aerodynamic loads and thus to potentially catastrophic technological consequences. Because of its dramatic impact on several applications, a considerable number of researches have extensively studied these phenomena in the past.[1–6] Indeed, dynamic stall can affect the performance and operational limits of many engineering and aeronautical applications, such as helicopters, highly manoeuvrable aircraft, and wind turbines. The aim of dynamic stall research varies for each application. For example, while on the helicopter blades the objective is mainly to inhibit the formation of the dynamic stall vortex, on fixed wing aircraft, the idea could be to sustain the lift overshoot generated by the dynamic stall vortex formation to enhance the manoeuvrability.

So far, experimental works have mainly focused on unsteady flows over two-dimensional aerofoils undergoing prescribed pitching motions.[1–5,7–11] Most of these works[1–3,7–10] have also investigated the influence on the aerodynamic response of various parameters, such as aerofoil geometry, Reynolds and Mach numbers, oscillation amplitude, and frequency. Halfman *et al.*[1] created a combined experimental and theoretical method able to predict the effect of the dynamic stall on the aerodynamic load. This approach was further developed by Ericsson and Reding.[7–10] McCroskey[2,3] described the main physical features of the phenomenon and classified the dynamic stall into two categories: light and deep stall, the former being characterised by a loss of lift and an increase in drag which are of the same magnitude as the one associated with the classical static stall, and by a size of the separated region in the order of the aerofoil thickness. Conversely, deep stall is characterised by a lift overshoot, due to the passage of a large scale vortex over the suction side of the aerofoil, followed by a lift breakdown associated with the vortex detachment. Deep stall is

also characterised by a separated region with a size in the order of the aerofoil chord. Shih *et al.*,[12] using particle image velocimetry visualisations, suggested that the main stall vortex is induced by the early boundary layer separation near the leading-edge of the aerofoil, and that full stall occurs when the boundary layer detaches completely from the aerofoil. Acharya and Metwally[13] have highlighted the presence of two pressure peaks in the forward portion of the aerofoil. The first suction peak grows in magnitude as the aerofoil pitches up, while the second one corresponds to the dynamic stall vortex and moves downstream.

High fidelity numerical simulations of dynamic stall in configuration of aeronautical interest are particularly expensive due to the broad range of time and space scales involved in the phenomenon: the unsteady variations of the angle of attack become slower and slower compared to the fastest turbulence time scale as the Reynolds number is increased. For this reason, Direct Numerical Simulation and Large Eddy Simulation (DNS and LES) are confined to low/intermediate Reynolds numbers while higher Reynolds simulations are normally dealt with Reynolds-Averaged Navier-Stokes (RANS) simulations. However, conventional turbulence models are known to fail in producing reliable solutions in such complex, out of equilibrium conditions: unsteady, recirculating and locally transitional flow.

A complete review on the numerical simulations of dynamic stall[14–20] can be found in the work of Ekaterinaris and Platzer.[21] One of the major outcomes of this survey is a list of research topics that required further advancements for achieving reliable predictions. Several other works have highlighted the difficulties that RANS calculations encounter when dealing with dynamic stall. In particular, Wang *et al.*[18] used two variants of the $k-\omega$ model, the standard and the SST one, to simulate the flow at moderate high Reynolds number $Re_c = 10^5$. From a comparison with experimental results, they noticed that the models cannot precisely capture the size and position of the dynamic stall vortex. Moreover, the quality of the predictions of the models deteriorates as the angle of attack increases. Dumlupinar and Murthy[19] further investigated the performances of various turbulence models and pointed out that different turbulence closures predict a broad range of different behaviours even in the light stall case.

Although several experimental and numerical studies have contributed in elucidating the main physical mechanism that comes into play on the flow behaviour when the angle of attack undergoes a dynamic change, to our knowledge the only high fidelity numerical simulations (i.e., DNS or resolved LES) which have been carried out so far are the implicit large eddy simulations of a pitching aerofoil undertaken by Visbal.[22,23] Those simulations can be considered to be a pioneering work aimed towards a more detailed understanding of the physical mechanisms that determine the dynamic stall vortex creation and its detachment. The understanding of this basic phenomenon would enable to devise new strategies and devices to control the changes in the aerodynamic loads. In this work, for the very first time, we aim at performing a direct numerical simulation of the transitional flow around an aerofoil in ramp-up motion. In a companion simulation, we also study the flow in a fully separated condition (at the same maximum angle of attack) to establish a baseline benchmark case to allow a cross comparison between the aerodynamic behaviour in a static and dynamic stalled condition.

Section II introduces the numerical formulation and the problem setup employed in this work, as well as the initial validation campaign. In Sec. III, we present our original contribution, first by discussing the fully separated flow at a static angle of attack, and later on by analysing the flow during a ramp-up motion. In this dynamic case, the angle of attack is varied at a constant rate until a maximum incidence of 20° is achieved. Finally, Sec. IV summarizes our main findings and draws some conclusions.

II. MATHEMATICAL AND NUMERICAL FORMULATION

To tackle the problem at hand, we consider an incompressible three-dimensional unsteady flow field, governed by the Navier-Stokes equations around a straight wing with an infinite spanwise dimension z (x_3). The computational domain is shown in Figure 1(a). The coordinate system is Cartesian with the x and y axes (x_1 and x_2) denoting the directions parallel and normal to the

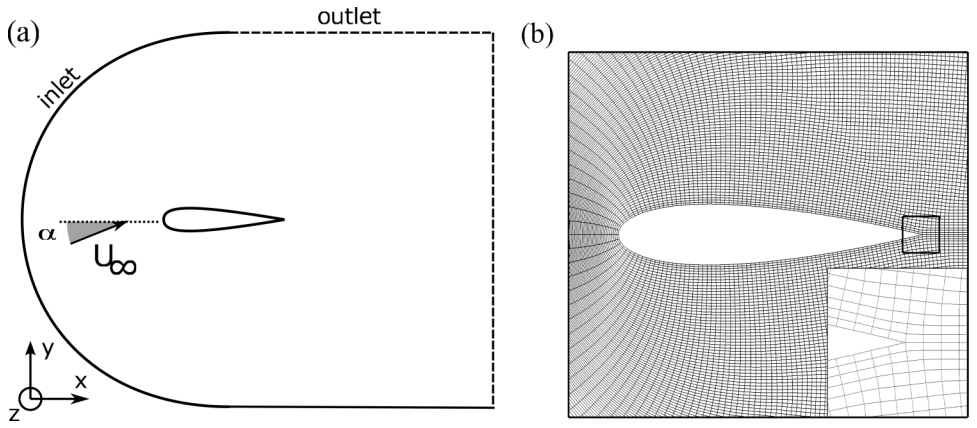

FIG. 1. (a) Sketch of the computational domain. (b) Grid in the proximity of the aerofoil (nodes are plotted with a skip index of six). The inserted figure is an enlargement of the area surrounding the trailing edge.

aerofoil chord, respectively. Also, u, v, and w (u_1, u_2, and u_3) denote the correspondent components of the velocity vector field parallel and normal to the chord, and along the span. In an inertial, Cartesian frame of reference, the dimensionless momentum and mass conservation equations for an incompressible flow read as

$$\frac{\partial u_i}{\partial t} + \frac{\partial u_i u_j}{\partial x_j} = -\frac{\partial P}{\partial x_i} + \frac{1}{Re_\infty}\frac{\partial^2 u_i}{\partial x_j \partial x_j}, \tag{1}$$

$$\frac{\partial u_i}{\partial x_i} = 0, \tag{2}$$

where $Re = U_\infty c/\nu$ is the Reynolds number based on the chord length of the aerofoil c and the approaching free-stream velocity magnitude U_∞ (ν being the kinematic viscosity). Einstein's summation notation applies. Unless otherwise stated, we use U_∞ and c as the velocity and length scales for normalisation throughout the paper.

Equations (1) and (2) are discretised on a collocated grid using a well-established curvilinear finite volume code.[24,25] The fluxes are approximated by a second-order central formulation, and the method of Rhie and Chow[26] is used to avoid pressure oscillations. The equations are advanced in time by a second-order semi-implicit fractional-step procedure,[27] where the implicit Crank-Nicolson scheme is used for the wall normal diffusive terms, and the explicit Adams-Bashforth scheme is employed for all the other terms. The Poisson pressure equation obtained when using a pressure correction method to enforce the solenoidal condition on the velocity field is transformed into a series of two-dimensional Helmholtz equations in wave number space via Fast Fourier transform (FFT) in the spanwise direction. Each of the resultant elliptic $2D$ problem is then solved using a preconditioned Krylov method (PETSc library[28]). In particular, for the problem at hand, we have found the iterative Biconjugate Gradient Stabilized (BiCGStab) method with an algebraic multigrid preconditioner (boomerAMG)[29] to behave quite efficiently. The code is parallelized using the domain decomposition technique and the MPI message passing library. Further details on the code, its parallelisation and the extensive validation campaign that have been carried out in the past can be found in Refs. 24, 25, and 30.

The aerofoil that has been selected for the present study is a symmetric NACA0020. The flow domain around the aerofoil is meshed using a body fitted C grid arrangement, as in Figure 1(b). The grid system for the three dimensional case is obtained by repeating the baseline $2D$ grid uniformly in the spanwise direction. With this arrangement, the external surface that bounds the computational domain contains both the inlet and the outlet (see Figure 1(a)). To determine which portion of the boundary in all parallel x-y planes is either an inlet or an outlet, at each time step a local spanwise average of the fluid velocity is evaluated in a tiny region close to the boundary. When the averaged flow direction points outward, the corresponding portion of the boundary is assumed to be an outlet and is treated using a convective boundary condition. Conversely, if the flow direction is directed

inward, the corresponding boundary surface is considered to be an inlet, and a Dirichlet type condition based on an irrotational approximation is employed. In particular, the values to be assigned to the velocity on the Dirichlet portions of the boundary are determined by solving a companion potential equation discretised via a Hess-Smith panel method.[31]

The Dirichlet inlet conditions are also modified in time to keep into account the change in incidence of the incoming velocity field. The approach that has been chosen to represent the time variation of the angle of attack is somehow controversial, since it does not reproduce standard wind tunnel experiments where the aerofoil is rotated around a revolution axis (usually the line through the centre of pressure of the aerofoil). However, the two approaches lead to similar results in terms of integral quantities, with some discrepancy in the shape and evolution of the wake (see Wong *et al.*[32]).

Finally, the remaining boundary conditions are imposed by enforcing: impermeability and no slip conditions on the aerofoil wall, periodic conditions on the planes bounding the domain in the spanwise direction, and continuity of the flow variables through the top and bottom planes generated by the C-grid shape downstream of the trailing edge.

All the simulations have been undertaken by fixing the Reynolds number based on the magnitude of the freestream velocity and the chord length to 20 000. The angle of attack is kept at 20° in the static case and varies according to a ramp function from 0° to 20° with a rate of change equal to $\dot{\alpha} = 0.12U_\infty/c$ in the linearly growing region of the ramp function.

We conclude this section by giving more details on the grid system. The mesh in Figure 1(b) has been generated in the xy-plane with particular care to its orthogonality and stretching features using the commercial software Pointwise,[33] with hyperbolic PDE extrusion methods. The resulting grid has a minimum included angle (83.19°) exactly matching the geometrical constraint of the trailing edge, see Figure 1(b), while the average grid included angle in all the domain is equal to 89.97. In the wall normal direction, the grid is almost uniform from the aerofoil surface up to 3 chords in order to capture all the separated region and the wake at high Reynolds number. Further away from the surface, it is coarsened with an increasing stretching factor, which maximum is located near the external boundary where it is equal to 1.03. In the direction parallel to the aerofoil, the grid is uniform over the wing and very slightly stretched (1.001) in the wake region. A buffer layer with higher stretching factor (1.015) is used near the outlet to suppress reflections. The three dimensional mesh is then obtained by repeating the two dimension grid in the spanwise direction with uniform spacing.

The grid density has been tuned by considering a number of preliminary two and three dimensional simulations. The former allowed us to establish the grid spacing requirements in the laminar portion of the flow featuring separation and convective instabilities. The latter was used to determine the grid resolution requirements in the turbulent flow regions. Through these preliminary simulations, undertaken at various incidence angles, we have found that a grid with $2785 \times 626 \times 97$ nodes in the x_1, x_2, and x_3 directions, respectively, delivered a sound resolution compromise throughout the whole incidence range. We also made sure that, in terms of local wall units, the corresponding mesh resolution verifies $\Delta x^+ < 3.0$, $\Delta y^+ < 0.5$, and $\Delta z^+ < 7.5$ where the superscript + indicates values made non-dimensional using the viscous length ν/u_τ and the friction velocity $u_\tau = \sqrt{\tau_w/\rho}$ (see Figure 2(a)). The grid dependency of the results has been evaluated by considering the first and second order statistics. In particular, we have tested a coarser and a finer

FIG. 2. (a) Mesh resolution at the wall. The resolution in the x, y, and z directions is shown with a solid, dashed, and dashed-dotted line, respectively. (b) Span-wise two-point correlation of the u velocity component in the near wake region.

FIG. 3. (a) Distribution of the mean pressure coefficient over the NACA 0012 aerofoil at 5° (triangle) and 8° (circle). (b) Mean x-velocity profiles at 8°. The profiles are at $x/c = 0.7$, 0.8, 0.9, 1.0, and 1.2. In both figures, the solid lines are from the actual simulations, while symbols are used for the results from Lehmkuhl *et al.*[34]

grid obtained by decreasing and increasing by 30% the number of grid points in all the three directions. The comparison between the medium and finer grid showed no significant differences.

Finally, concerning the spanwise size of the domain, its adequacy to contain the largest scales of the flow has been determined by comparing the spanwise two-point correlation at various xy coordinates. The two-point correlation is defined as follows:

$$R_{ii}(\boldsymbol{x},\boldsymbol{r}) = \frac{\overline{u_i'(\boldsymbol{x})u_i'(\boldsymbol{x}+\boldsymbol{r})}}{\overline{u_i'^2(\boldsymbol{x})}}, \tag{3}$$

where the bar denotes average over time and homogeneous direction z. The computed two-point correlation, shown in Figure 2(b), becomes negligible when approaching $0.13c$, less than half of the domain size ($0.45c$), which guarantees a good decorrelation between the periodic end planes.

A. Validation

The code has been extensively validated for turbulent flows.[24,25,30] However, to further corroborate the predictive capabilities of the code, we report a new validation of the flow over an aerofoil, where we compare our numerical results with the ones obtained by Lehmkuhl *et al.*[34] and by Rodriguez *et al.*[35] In particular, we have considered a NACA 0012 aerofoil at a chord Reynolds number $Re_c = 5 \times 10^4$ at angles of attack $\alpha = 5°$ and $\alpha = 8°$. The simulation domain has been set up and discretised with the same procedure previously described. We have used a grid of $2545 \times 490 \times 48$ points in the x_1, x_2, and x_3 directions, with a reduced spanwise extent of the domain (set to $0.2c$, as in Ref. 35).

The comparison with the reference data turns out to be quite satisfactory. Figure 3(a) shows the pressure coefficient distribution over the aerofoil surface at the two angles of attack obtained in the present simulations versus the ones given in Ref. 34. At both angles of attack all the predictions show the presence of a separation bubble on the suction side of the aerofoil, resulting in a plateau in the pressure coefficient. At $\alpha = 5°$, the flow separates at $x_s \approx 0.10c$ and reattaches at $x_r \approx 0.57c$, while at $\alpha = 8°$, the separation occurs at $x_s \approx 0.03c$ and the reattachment at $x_r \approx 0.30c$. A quantitative comparison with the results by Lehmkuhl *et al.*[34] is given in Table I. In general, we

TABLE I. Aerodynamic coefficients, and separation and reattachment points for the cases analysed. The data from the first two rows are taken from Lehmkuhl *et al.*[34]

Case	Aerofoil	Re_c	α (deg)	C_L	C_D	x_s/c	x_r/c
Val-5-Ref	NACA0012	5×10^4	5	0.57	0.029	0.065	0.57
Val-8-Ref	NACA0012	5×10^4	8	0.76	0.050	0.024	0.32
Val-5	NACA0012	5×10^4	5	0.57	0.028	0.100	0.57
Val-8	NACA0012	5×10^4	8	0.73	0.049	0.032	0.30
Stall-20	NACA0020	2×10^4	20	0.64	0.35	0.025	...

find an overall good agreement in the results, with a slightly retarded separation in our simulations. Figure 3(b) shows the mean x-velocity profiles in the vicinity of the trailing-edge and in the near wake region at $\alpha = 8°$. Again, good agreement with the results from the reference is observed.

III. RESULTS AND DISCUSSION

A. High angle of attack

We now consider the flow over the NACA 0020 aerofoil at an angle of incidence of 20°. The flow statistics have been collected during $100c/U_\infty$ time units after the initial transient. Averaging in the spanwise homogeneous direction and over 100 external time units (based on c and U_∞) was largely sufficient to produce statistically steady results. The mean x-velocity component is shown in Figure 4(a), together with the pressure coefficient C_p (Figure 4(b)) and the friction coefficient C_f (Figure 4(c)). From the mean velocity isocontours in Figure 4(a), it clearly appears that the aerofoil is in a fully stalled condition with a large recirculation zone present on the whole suction side. The separation bubble occupies a volume of $0.5c$ in the y-direction and $0.3c$ in the x-direction behind the trailing edge, where a secondary recirculation appears. The primary recirculation zone generates a plateau in the pressure coefficient (Figure 4(b)) which extends on the whole suction side after a small suction peak near the leading edge, while the reduced pressure region at the trailing edge is due to the secondary recirculation. Another smaller recirculation bubble is visible at $0.25c$ centred in proximity of the location of the aerofoil maximum thickness. The presence of this separation bubble, extending from $x = 0.15c$ to $x = 0.50c$, can also be educed from the friction coefficient distribution (Figure 4(c)). Figure 4(a) also shows u-velocity profiles in 3 different positions along the chord (at the leading edge $x = 0.0c$, at the mid chord $x = 0.5c$, and at the trailing edge $x = 1.0c$) and further downstream in a location within the wake ($x = 1.5c$). The given profiles show that at the leading edge, the flow is attached and the boundary layer starts developing with a strong adverse pressure gradient (Figure 4(b)) that results into separation of the flow at $x = 0.025c$; at mid chord the flow is reversed near the aerofoil and, after attaining a maximum negative velocity value at $y = 0.15c$, it grows until reaching zero value at $y = 0.26c$; at the trailing edge, the x-velocity component becomes zero at $y = 0.04c$ after having formed a tiny shear layer with positive velocity, and further away from the aerofoil it reaches the value $-0.29U_\infty$ (close to the absolute minimum in

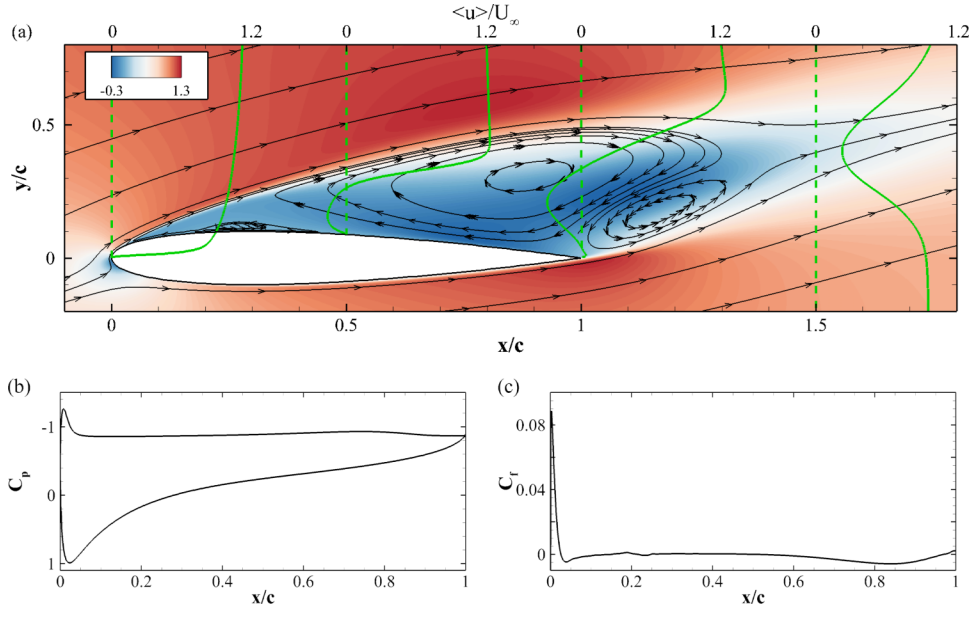

FIG. 4. (a) Contours of mean flow x velocity and streamlines, (b) pressure, and (c) friction coefficient of NACA 0020 aerofoil at an angle of attack $\alpha = 20°$ and with a Reynolds number $Re_c = 2 \times 10^4$.

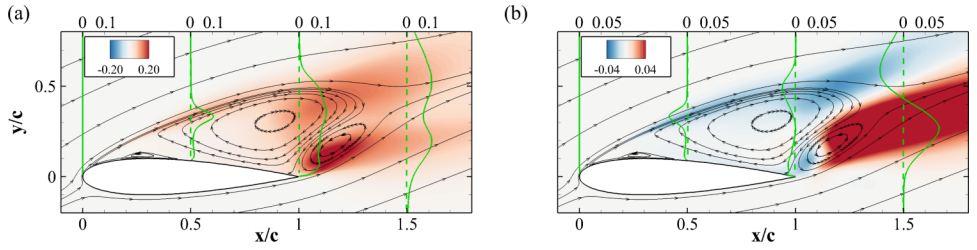

FIG. 5. (a) Contours of tangent $\langle u_t' u_t' \rangle / U_\infty^2$ and (b) shear $\langle u_t' u_n' \rangle / U_\infty^2$ components of the Reynolds stress tensor. Mean flow streamlines and some profiles are also shown.

the whole domain) at $y = 0.21c$, to recover again a zero value at $y = 0.33c$. Finally, the last profile shows the velocity profile within the wake, featuring a characteristic defect shape and a positive minimum value $0.22U_\infty$ reached at $y = 0.40c$.

Figure 5 shows the diagonal $u_t' u_t'$ (Figure 5(a)) and off diagonal $u_t' u_n'$ (Figure 5(b)) components of the Reynolds stress tensor, where u_t and u_n are the fluctuating velocity components tangent and normal to the free-stream velocity direction, respectively. High values of the stresses are present in the wake behind the aerofoil, and in other two regions: within a tiny shear layer originating from the leading edge which bounds the clockwise recirculating region, and behind the trailing edge where the anti-clockwise recirculation takes place. All the Reynolds stresses vanish at the wall due to the no-slip condition and far from the aerofoil surface where the flow is laminar. One can also notice that the approaching flow is laminar, as shown by the 0 values of the stresses profile at the leading edge. At $x = 0.5c$ the stresses have low intensities in the recirculating region near the wall, and then form a peak located at $y = 0.12c$. In the wake behind the trailing edge, the Reynolds stresses have two peaks located at $y = 0.26c$ and $0.59c$, the first peak having a higher intensity than the second. The high stress intensity in the wake zone is mainly due to the flow separation taking place at the trailing edge of the aerofoil, with a smaller contribution from the shear layer formed at the leading edge. Both these regions are responsible to shed vorticity of opposite sign in the wake, carrying different contributions in terms of intensities and thus breaking the symmetry of the wake.

Figure 6(a) shows the lift and drag coefficients as a function of time. These distributions have been obtained by integrating the pressure and shear stress at the wall. Their mean values are $C_L = 0.64$ and $C_D = 0.35$, respectively. These values, compared with the ones reported by Skillen *et al.*,[36] obtained via a large eddy simulation of the flow around a similar aerofoil at same incidence but at higher Reynolds number, show small discrepancies with slightly higher lift (3%) and drag (6%) coefficients. From the figure, it is also possible to notice the presence of a dominant frequency. This frequency corresponds to the shedding of vortices in the wake, and its nondimensional value in terms of Strouhal number is $St = f_s c / U_\infty \approx 0.534$. An alternative Strouhal number based on the windward length $c \sin(\alpha)$ gives a value of $St' = f_s c \sin(\alpha) / U_\infty = 0.183$. This value falls within the range 0.175–0.185 in agreement with the results of Knisely[37] that also showed that the Strouhal number tends to become independent of the shape of the bluff object when the angle of attack is increased. To further investigate the unsteady nature of the flow field and, in particular, aiming at tracing the footprint of the vortex generation process originating from the shear layer instability

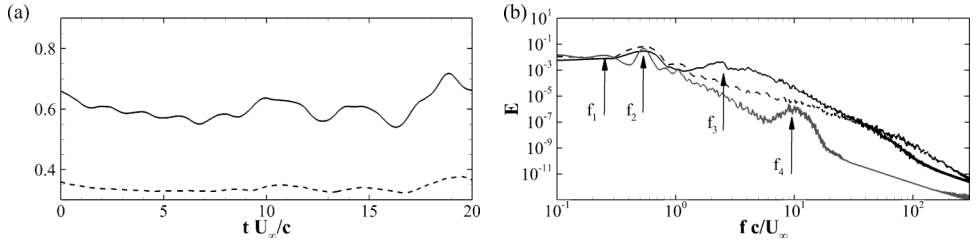

FIG. 6. (a) Lift C_L (solid line) and drag C_D (dashed line) coefficients as a function of time. (b) Spectra of the time autocorrelation of the u velocity component at points P01 (gray solid line), P02 (black solid line), and P03 (dashed line).

at the leading edge, we have computed the spectrum of the time autocorrelation at three different locations (Figure 6(b)) (P01, P02, and P03). The first one (P01) is located in the shear layer close to the leading edge at $x = 0.10c$, $y = 0.10c$, the second one (P02) in the shear layer near the midchord at $x = 0.40c$, $y = 0.28c$, and the last (P03) near the trailing edge at $x = 1.05c$, $y = 0.08c$. All the spectra show a peak at $St = 0.534$ which is the reported principal wake shedding frequency (f_2). In the shear layer near the leading edge (P01), we observed a peak at lower frequency $f_1 = 0.25U_\infty/c$, corresponding to approximately half the shedding frequency and related to a low frequency flapping motion of the shear layer.[35,38–41] In the same spectrum, a third peak is present at $f_4 = 9.75U_\infty/c$ corresponding to the vortex generation due to the leading edge Kelvin-Helmholtz (KH) shear layer instability. Another smooth peak at frequency $f_3 = 2.52U_\infty/c$ is present in the spectrum corresponding to the midchord location (P02). This frequency is lower than f_4 due to the merging of vortices which grows in size. An analogous trend can be observed in the work of Rodriguez *et al.*[35]

More details on the emerging coherent structures, their interactions, and the wake formation process have been educed using the Q-criterion proposed by Hunt *et al.*[42] This technique allocates a vortex to all spatial regions that verify the condition

$$Q = \frac{1}{2}\left(|\boldsymbol{\Omega}|^2 - |\boldsymbol{S}|^2\right) > 0, \tag{4}$$

where $\boldsymbol{S} = \frac{1}{2}\left(\boldsymbol{\nabla u} + \boldsymbol{\nabla u}^T\right)$ is the rate of strain tensor and $\boldsymbol{\Omega} = \frac{1}{2}\left(\boldsymbol{\nabla u} - \boldsymbol{\nabla u}^T\right)$ is the vorticity tensor. Instantaneous Q iso-surfaces are shown in Figure 7(a). From this figure, the principal flow features are easily observed: the laminar flow separates at the leading edge, forming a shear layer that rolls up into KH vortices;[43–47] this instability, locally, triggers the flow transition to turbulence; further downstream a turbulent separated region appears to be characterized by fine texture small-scales structures, which eventually merge into coherent larger structures; finally behind the aerofoil, a

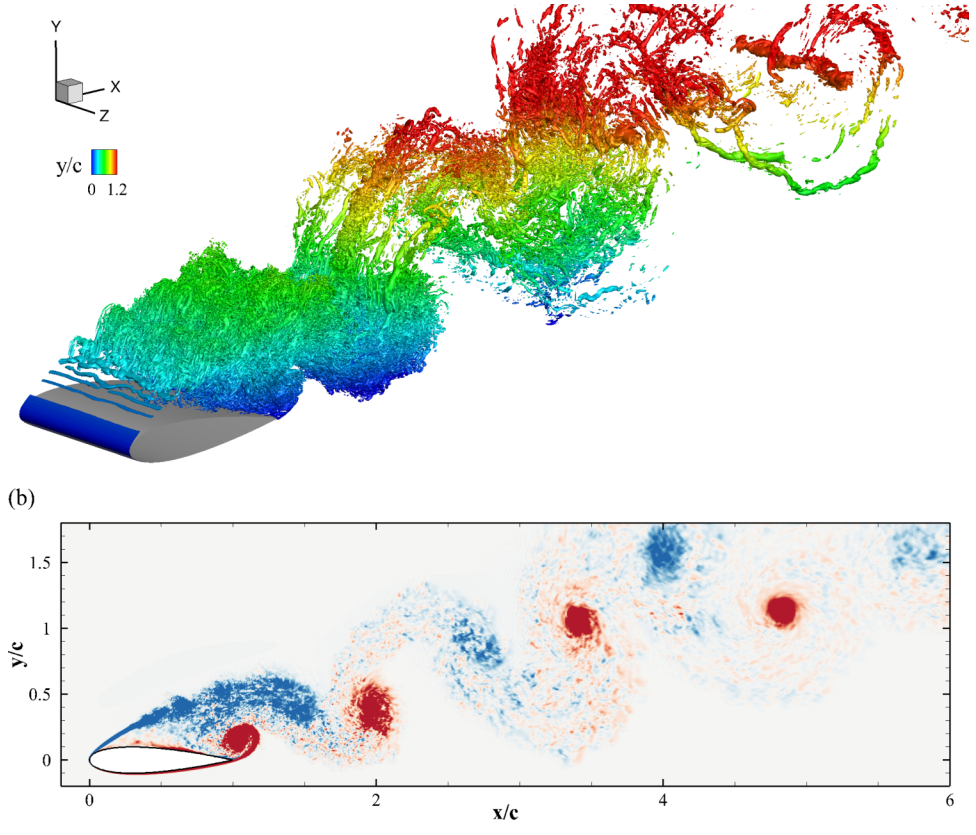

FIG. 7. (a) Visualisation of instantaneous vorticity field by means of Q-iso-surfaces ($Q = 150U_\infty^2/c^2$) coloured by the y-coordinate (distance from centreline). (b) Instantaneous contour plot of the spanwise component of the vorticity ω_z, averaged in the homogeneous z-direction. Blue negative vorticity, red positive ($\pm 7U_\infty/c$).

large turbulent wake is formed, whose shape is similar to a von Karman vortex street typical of bluff bodies, as clearly shown in Figure 7(b). However, in contrast to classical vortex shedding process showing an alternate series of vortices of opposite sign and equal strength, here the wake is highly asymmetric presenting vortices of uneven strength. As already mentioned, the loss of symmetry and the irregularity of the vortices pattern is related to the interaction between the two vortex generating mechanisms (see Breuer and Jovicic[48,49]): the vortices roll up under the action of the KH leading edge shear layer instability and the street of vortices characterising the wake behind the trailing edge. Figure 7(a) shows also the presence of braid-like vortices between each shedding rollers.

Within the Eulerian coherent structures educing techniques, the Q-criterion is probably the most popular one. Even though it enjoys the Galilean invariance property, it has other shortcomings that are typical of Eulerian methods: it lacks objectivity (i.e., not independent of frame rotations), it is based on the numerical evaluation of gradients that may introduce further noise, and it requires the empirical specification of a threshold value. On the other hand, methods that are based on a Lagrangian formulation overcome those weaknesses. In particular, one of the most popular Lagrangian approaches is based on computing the Finite-Time Lyapunov Exponents (FTLE) (see Haller[50] and Shadden *et al.*[51]). The FTLE $\sigma^T(\boldsymbol{x},t)$ is a scalar function of space and time which measures the rate of separation of neighbouring particle trajectories initialised within a small ball centred at $\boldsymbol{x}$ at time t. More precisely, if $\boldsymbol{x}(t,\boldsymbol{x}_0,t_0)$ denotes the position of a particle at time t that originated from position $\boldsymbol{x}_0$ at time t_0, a measure of particles separation rate can be related to the largest singular value of the Cauchy-Green deformation tensor computed over a finite time interval $[t_0,t_0+T]$,

$$\Delta = \frac{\partial \boldsymbol{x}(t_0+T,\boldsymbol{x}_0,t_0)}{\partial \boldsymbol{x}_0}. \tag{5}$$

Once the largest singular value $\lambda_{max}(\Delta)$ is found, the FTLE over the time interval $[t_0,t_0+T]$ is defined as

$$\sigma^T(x,t) = \frac{1}{T}\ln\sqrt{\lambda_{max}(\Delta)}. \tag{6}$$

One can use both positive and negative integration times to evince either attracting Lagrangian Coherent Structures (LCS, unstable manifolds) with negative integration time $T<0$, or repelling LCS (stable manifolds) characterised by positive integration time $T>0$.[52] LCS are, therefore, used to classify regions in the flow undergoing different dynamical conditions. In particular, the recirculating regions are identified by their association with unstable LCS. Figure 8 shows contours of the FTLE, where the coherent structures are associated to local extrema of σ^T. The six different instantaneous snapshots considered in the figure cover a full shedding period $\Delta t = 1.75c/U_\infty$ (see Figure 6(a)). Figure 8(a) corresponds to the beginning of the shedding cycle, with no vortex at the trailing edge, and the leading edge shear layer rolling up under the action of a Kelvin-Helmholtz instability. Later on (Figure 8(b)), also the trailing edge shear layer undergoes a KH instability rolling up and inducing the generation of a trailing edge vortex. In the following instantaneous snapshots, the trailing edge vortex increases in size (Figures 8(c) and 8(d)), interfering with the leading edge KH instability also affecting the thickness and the location of the shear layer. This interaction continues until the trailing edge vortex is fully established and detaches from the aerofoil (Figure 8(e)). As the trailing edge vortex is convected downstream (Figure 8(f)), the leading edge shear layer is no more drawn into the separated region, and the undisturbed KH instability process associated with the leading edge induced shear layer is recovered. Ultimately, this cyclic interaction between the leading and trailing shear layers is the responsible of the asymmetry in the wake pattern. At the trailing edge, vortices generated by the flow separation from the aerofoil surface are shed into the wake, while the small scale vortices generated by the Kelvin-Helmholtz instability of the shear layer at the leading edge are periodically either trapped in the recirculating bubble or shed into the wake also increasing their size via a pairing process.

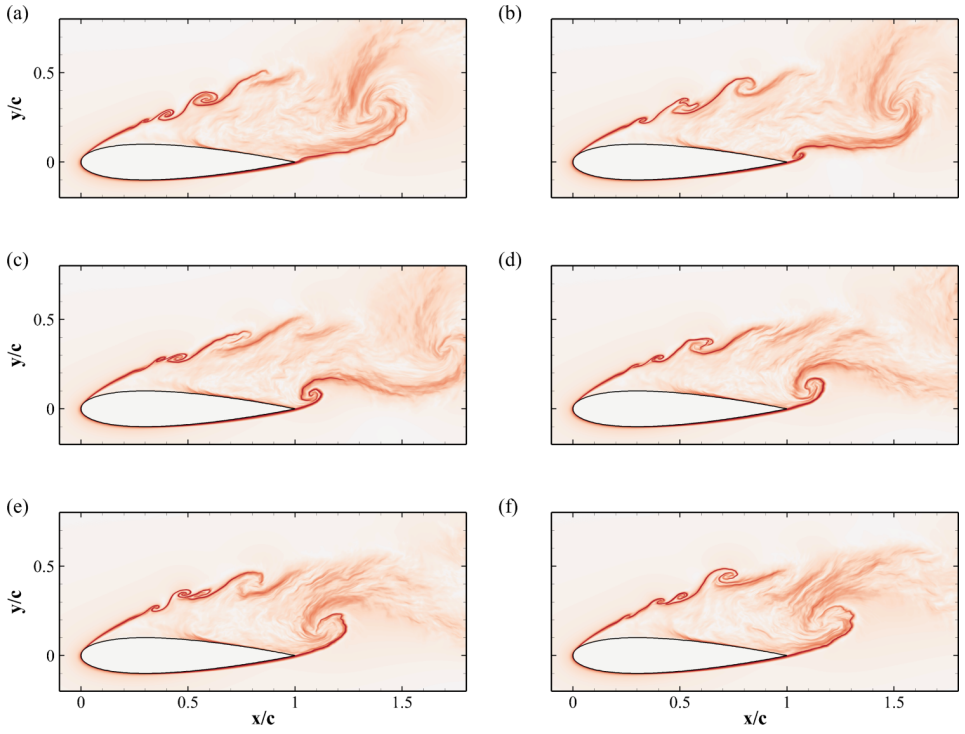

FIG. 8. Instantaneous contour plot of the FTLE σ^T (defined in (6)) during a shedding period. Snapshots have been sampled at 6 time instantaneous snapshots by an increment $\Delta T \approx 0.35c/U_\infty$. Darker colours are associated with most unstable LCS. The contour levels go from 0 (white) to $7U_\infty/c$ (red).

B. Ramp-up

We now consider the evolution of the flow field around the aerofoil during a ramp-up motion. As already mentioned, in this manoeuvre, the angle of attack follows a ramp function in time with an initial linear increase followed by a steady value of the angle. In particular, the angle of attack is varied linearly from 0° to 20° with a reduced frequency of $k = \dot{\alpha} = 0.12U_\infty/c$. These values have been selected because matching the experimental conditions of Brucker and Weidner[6] (the reduced frequency is also very close to the one of Mulleners and Raffel[4]). The simulations are initialized from a fully developed zero degree angle of attack flow condition. Because of the intrinsic unsteady nature of the flow field, time averaged statistics can no more be defined, and only averages in the homogeneous z-direction can be used. Convergence of the flow statistical quantities has been enhanced by also introducing ensemble averages obtained from different initial conditions. In particular, we have considered ten realisations obtained using ten initial conditions obtained from instantaneous zero degree flow fields sampled within two shedding cycles. Flow statistics obtained using ensemble averages and span wise planes were fairly converged.

Figure 9(a) shows the time history of the lift and drag coefficients during the ramp-up motion (solid lines), compared to the case at fixed angle of attack $\alpha = 20°$ (dashed lines). From the force coefficients diagram, we can easily recognise the typical stages of dynamic stall, as described, for example, by McCroskey.[2] The lift and drag coefficients first increase until reaching maximum values after the end of the linear increase of the angle of attack. Due to the passage of a large scale vortex over the suction side of the aerofoil, the magnitude of the maxima is larger than the static stall values. As this vortex detaches, the force drops abruptly. Finally, they oscillate slowly converging towards the asymptotic static stall values. The maximum lift and drag coefficients are 1.58 and 0.67, respectively, about twice the values of the static case. In the decaying region, the amplitude of the oscillations is much higher than in the static case, while the characteristic shedding frequency is lower in the ramp-up case. Those differences between the dynamic and the static cases become less accentuate approaching the asymptotic state.

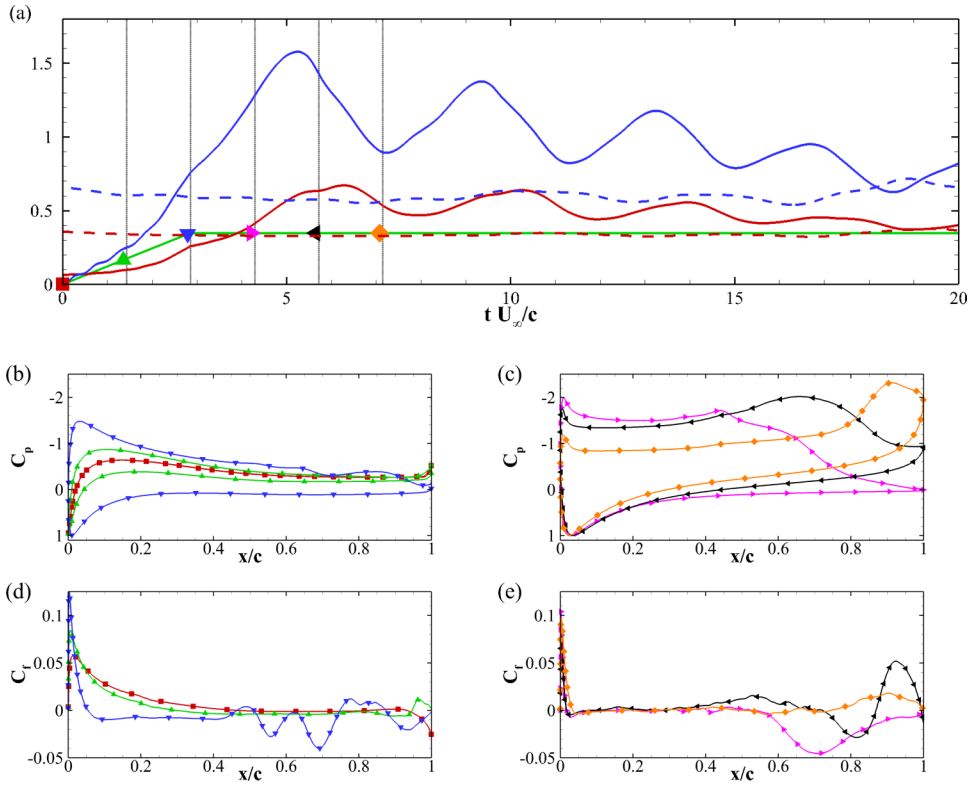

FIG. 9. (a) Lift (blue line) and drag (red line) coefficient over time, with the selection of 6 particular times indicated by the dashed line and the symbols. The solid line is used for the ramp-up case, while the dashed line is for the case at $\alpha = 20°$. (b) and (c) Pressure coefficient C_p and (d) and (e) friction coefficient C_f at the selected times.

Figures 9(b)–9(e) show the time evolution of the pressure and friction coefficients, C_p and C_f, and Figure 10 displays the contours of the span-wise z-component of vorticity ω_z, averaged in the span-wise homogeneous z-direction, sampled at the same six times as the corresponding C_p and C_f distributions (i.e., the six time instants marked in Figure 9(a)), with the first corresponding to $\alpha = 0°$, the second to $\alpha = 10°$, and the others to $\alpha = 20°$. At $\alpha = 0°$, the C_p distribution is symmetric (Figure 9(b)), with a plateau starting at about the mid-chord position, indicating the presence of a separated region. The rightmost local minimum located by the trailing edge is induced by vortex shedding. The friction coefficient on the suction side of the aerofoil confirms the mentioned boundary layer features, displaying a peak near the leading edge, followed by a smooth decrease (Figure 9(d)) and the presence of the separation point at about the mid-chord. The flow is symmetric over most of the aerofoil surface (Figure 10(a)), except at the trailing edge and in the wake, where contra-rotating vortices are shed from the suction and pressure sides of the wing. As the angle of attack reaches the value of 10°, the pressure distribution (Figure 9(b)) and the flow (Figure 10(b)) are no more symmetric, and the lift starts to increase consequently. The maximum friction coefficient moves towards the leading edge, as well as the separation point (Figure 9(d)). When the static stall angle is reached, small amplitude C_f oscillations in the trailing edge area become visible. At $\alpha = 20°$, the lift is still increasing, consistently with the pressure decrease on the suction side (Figure 9(b)). Also, even if the separation point has now reached the static stall value, the pressure coefficient distribution does not show the typical separation plateau. Compared to the static case, the C_f oscillations take place further upstream towards the leading edge (Figure 9(d)). When the maximum lift coefficient is approached, the peak of the pressure near the leading-edge is still increasing, and a second peak appears around the mid-chord (Figure 9(c)). This new peak is induced by a large vortex which has started to form on the suction side (i.e., the so called dynamic stall vortex), see Figure 10(d). Further downstream, the pressure drops rapidly, while the friction coefficient (Figure 9(e)) reaches a maximum negative value. During this phase,

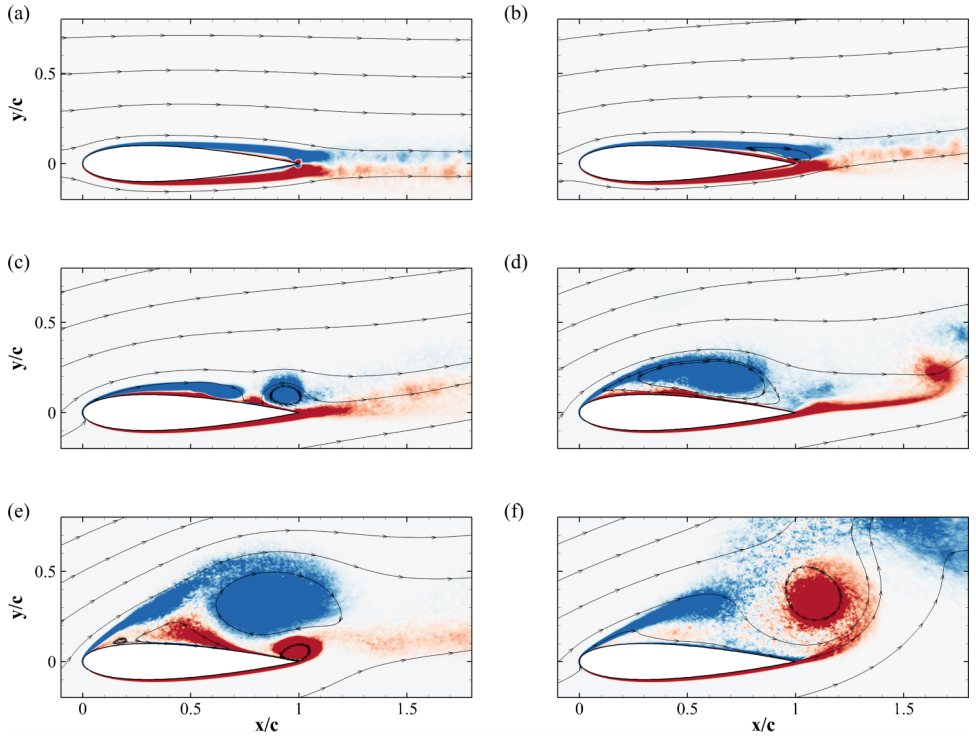

FIG. 10. Contour plots of the space and ensemble average of the spanwise component of vorticity ω_z, sampled at the times given in Figure 9(a). Blue negative vorticity, red positive ($\pm 7U_\infty/c$).

no vortices are shed from the trailing edge, as can be educed from Figure 10(d). In later stages, as shown in Figure 9(c), the pressure peak value at the leading edge starts to decrease, while the secondary peak intensity keeps on increasing in magnitude, moving towards the trailing edge, as the dynamic stall vortex is convected downstream. During the displacement of the dynamic stall vortex, an induced counter rotating vortex is formed at the trailing edge, see Figure 10(e). When the dynamic stall vortex finally detaches from the aerofoil and the trailing edge vortex reaches its maximum size (Figure 10(f)), the pressure attains an almost constant distribution indicating a fully separated flow condition (Figure 9(c)). However, the lift will then start to increase again due to the formation of another shed vortex, whose magnitude and intensity are weaker than the first one. This cyclic shedding process is damped in time with vortices of lower intensities until the static condition is asymptotically reached. The time evolution of the separation point is reported in Figure 11(a). At $\alpha = 0°$, the separation point is located at $x_s = 0.47c$, moving towards the leading edge as the angle of attack is increased. As already remarked, the static stall separation point $x_s = 0.025c$ is first reached when the ramp-up motion is finalised at $t = 3.5c/U_\infty$. In the subsequent stage, when the incidence angle is constant ($\alpha = 20°$), the separation line moves further upstream featuring a damped oscillating trajectory around its static location.

FIG. 11. (a) Time evolution of the downstream separation point during the ramp-up manoeuvre (solid line). The dashed line represents the separation point at 20°. (b) Fluctuations of the x-velocity components u' as a function of time for various points near the aerofoil surface. The fluctuations are scaled by a factor of 10 and shifted.

When commenting Figures 9(d) and 9(e), we have already highlighted the presence of some oscillations in the C_f distribution by the trailing edge region. These oscillations amplify in time affecting larger portions of the profile. The driving mechanism that trigger these oscillations is associated with a KH shear layer instability that starts at the trailing edge and propagates up-stream in time. This phenomenon is analysed in Figure 11(b) showing the evolution over time of the fluctuations of the stream-wise velocity component at various locations along the aerofoil suction side (as shown in the figure), at a wall normal distance of $0.1c$. The bullets used in the figure indicate the time when the amplitude of the fluctuation reaches the 2.5% of the average value. From this diagram, it appears clearly that initially the x-wise velocity fluctuations are confined to the trailing edge region. Only after 2 time units the fluctuations reach the half chord location. Later on they travel slowly further upstream, but never contaminating the leading edge portion of the aerofoil. Thus, it is clear that the separated region moves upstream in time, with an initial velocity approximately equal to $0.15U_\infty$.

Next, we focus on the time evolution of the turbulent kinetic energy $k = 1/2\,\langle u_i' u_i' \rangle$, shown in Figure 12, together with the corresponding mean streaklines. At $\alpha = 0°$ the flow accommodates smoothly around the aerofoil with low levels of turbulent kinetic energy confined in the wake behind the trailing edge. As the angle of attack is increased (Figures 12(b) and 12(c)), a recirculation zone is formed on the suction side of the aerofoil in the trailing edge region. At later stages, a complete separation occurs affecting the whole suction side (Figure 12(d)). The associated recirculation zone displays high levels of turbulent kinetic energy. The following time frame, Figure 12(e), shows a completely formed dynamic stall vortex that, later on, will be convected downstream towards the trailing edge. A new contra-rotating bubble is formed at the trailing edge, and other two recirculation regions appear, one at about the mid-chord location and the other around $x = 0.15c$. Both of them finally vanish when the dynamic stall and trailing edge vortices are shed away from the aerofoil (see Figure 12(f)).

To better understand the vortex formation and transport processes and the origin of the instabilities arising in the flow, we turn our attention to Figure 13 where the evolution of the FTLE

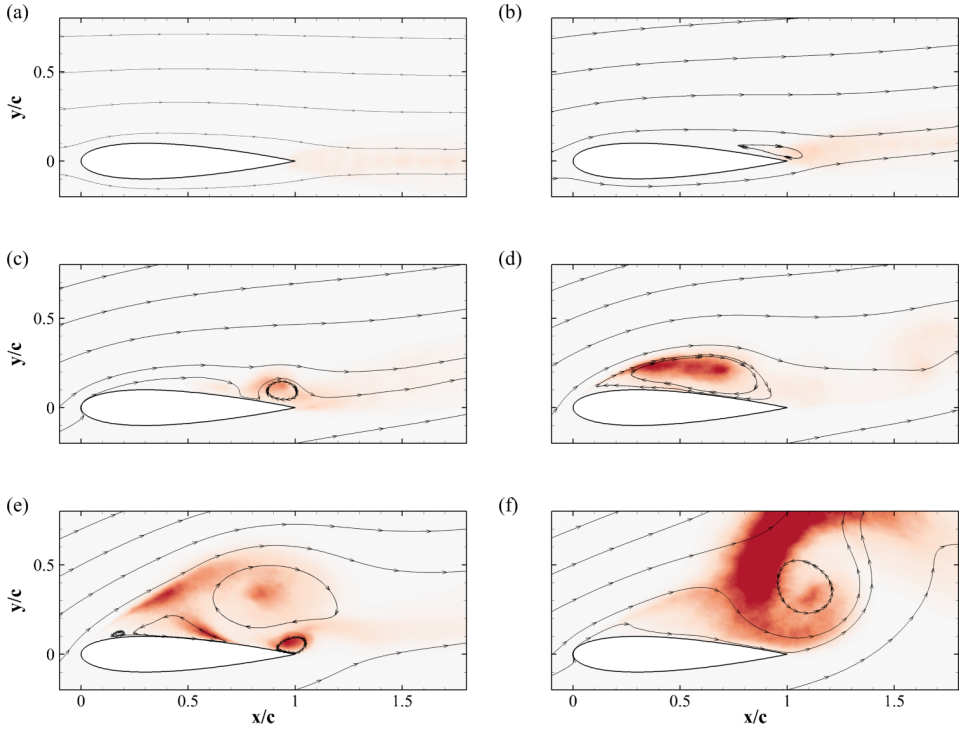

FIG. 12. Contour plots of the ensemble average among solutions with different initial conditions of the turbulent kinetic energy k, averaged in the homogeneous z-direction, at the times shown in Figure 9. The contour level goes from 0 (white) to $0.15U_\infty^2$ (red).

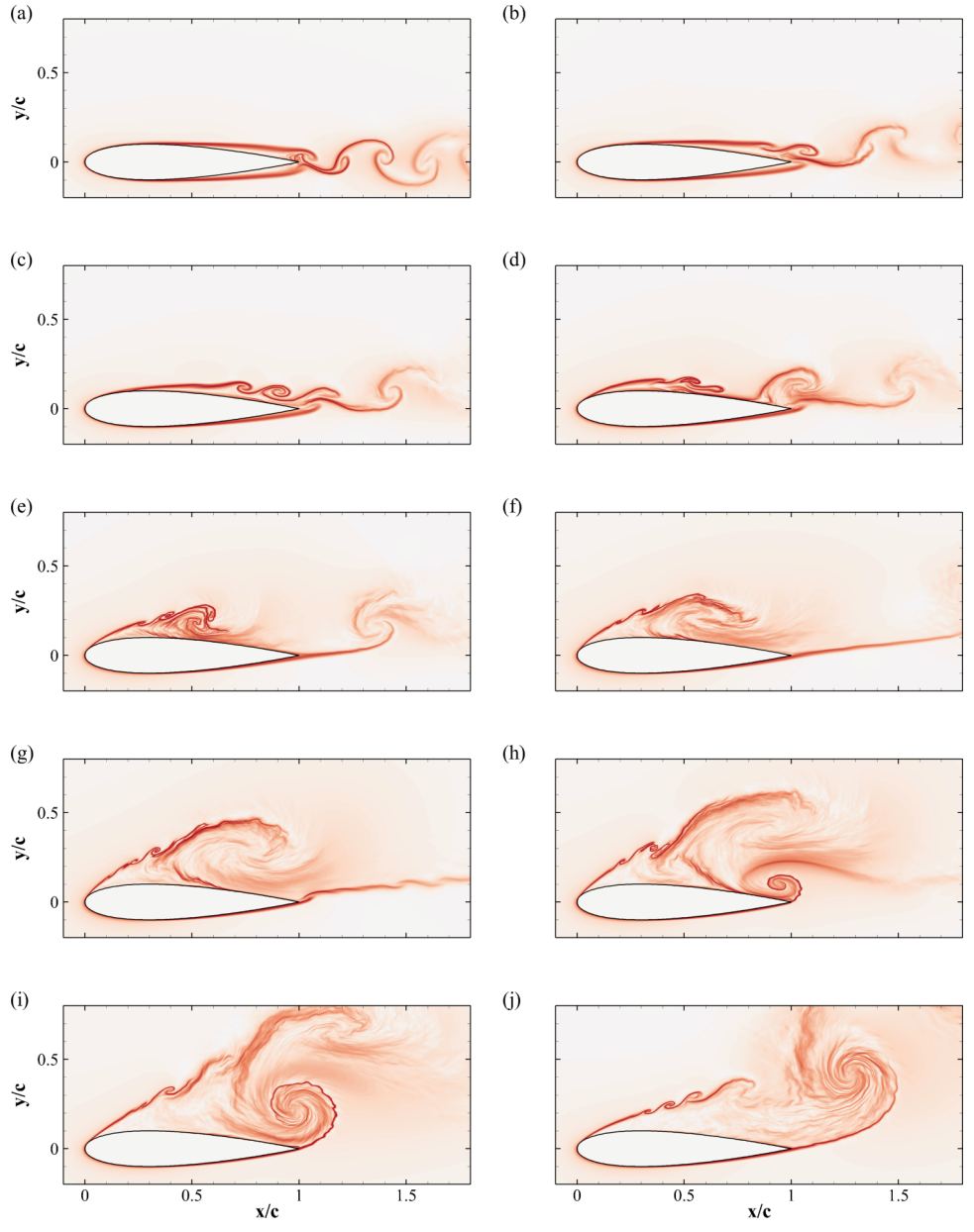

FIG. 13. Contour plot of the FTLE σ^T. Time increases from left to right and from top to bottom, with a sampling time interval of $\Delta t = 0.715c/U_\infty$. The initial time (a) corresponds to $\alpha = 5°$. The contour levels go from 0 (white) to $7U_\infty/c$ (red).

σ_t^T is reported. In the figure, the frames are organised time wise, with the right column covering the same instantaneous snapshots marked in Figure 9, while the left column displays contours at times sampled in-between. Figure 13(a) corresponds to the earliest stage at $t = 0.715c/U_\infty$, when the angle of attack is $\alpha = 5°$. Initially, in panel a, the flow is slightly asymmetric, with two shear layers developing around the mid-chord. In the next two panels (b and c), the flow on the pressure side tends to reattach, while the suction side shows an early separation with the trailing edge shear layer initiating to roll up, and shedding vortices at the trailing edge. At $\alpha = 20°$, the shear layer rolls-up into a recirculating region that closes at around the mid-chord (Figure 13(d)). This roll-up process continues (Figures 13(e) and 13(f)) leading to the formation of a large scale vortical structure, i.e., the dynamic stall vortex. As already noticed, while this large scale vortex is formed, no vortices are shed from the trailing edge and an almost straight shear layer is formed. The latter is

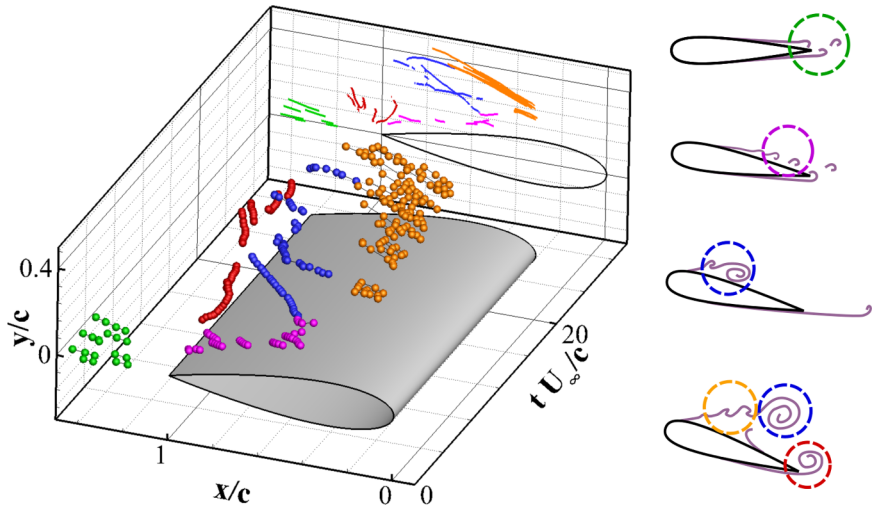

FIG. 14. Vortices positions as a function of time, and sketch of the main events occurring during the dynamic stall.

displaced towards the suction side and distorted by the clock-wise rotation of the dynamic stall vortex (Figure 13(g)), causing its fast roll-up (Figure 13(h)). The newly generated trailing edge vortex pushes the dynamic stall vortex upwards causing its detachment from the aerofoil while it grows in size (Figure 13(i)). Also the leading edge shear layer is influenced by the presence of the trailing edge vortex forming a larger angle with the chord. When the trailing edge vortex is shed, the leading edge shear layer moves again closer to the aerofoil (Figure 13(j)) and starts to roll-up forming a new vortex. This cycle is repeated for a few more times while the intensity of the vortex decays.

To better track the movement of the large scale coherent structures, we have also performed a supplementary vortex eduction study and tracked the cores of the vortices identified using the criterion proposed by Kida and Miura.[53] This methodology defines vortex cores in a two dimensional setting by checking on the correspondence of local pressure minima and the verification of a swirl condition. In particular, the criterion on the swirl reads as $\mathcal{S} < 0$, where $\mathcal{S}$ is the discriminant of the velocity gradient tensor in the plane, i.e., $\mathcal{S} = (\partial u/\partial x - \partial v/\partial y)^2/4 + \partial u/\partial y\, \partial v/\partial x$. To eliminate the noise induced by very low intensity vortices, we have pre-filtered all the vorticity contributions with span-wise vorticity values lower than $0.01U_\infty/c$. The evolution of the vortices trajectories, obtained by joining the space locations verifying the two criteria, is plotted in Figure 14. The vortices are classified into five groups, marked with different colors. At initial times, vortices are shed only at the trailing-edge (green), but as the separation point moves upstream (Figure 11), vortices start also to be shed from the suction side of the aerofoil at increasingly up-stream locations (magenta). Later, at $t \approx 4c/U_\infty$, the vortices at mid-chord start to merge and the dynamic stall vortex is formed (blue). The dynamic stall vortex first remains almost stationary in its position while it is formed, while later on it is convected downstream with a phase velocity of about $0.25U_\infty$. As the latter approaches the end of the aerofoil, the trailing edge vortex is generated (red). This newly formed vortex is first attracted towards the dynamic stall vortex upstream, and, when it is fully formed moves away from the aerofoil surface. Meanwhile, the leading edge shear layer keeps shedding vortices (yellow) which merge into other large scale structures.

IV. CONCLUSION

We have carried out a number of direct numerical simulations of the flow around a NACA 0020 aerofoil at a chord Reynolds number of $Re_\infty = 20\,000$, considering the variation of the incidence angle. After describing and validating the numerical approach with results from the literature, the flow around the aerofoil has been simulated in both a static stall condition at 20° and in a dynamic stall condition, with the angle of attack varying linearly from 0° to 20° at a non-dimensional rate of $\dot{\alpha}_{\mathrm{rad}} = 0.12U_\infty/c$.

In the static stall case, the flow is dominated by a large recirculation zone present on the whole suction side, with a secondary smaller recirculation bubble located in correspondence of the aerofoil maximum thickness. The shear layer formed at the leading edge undergoes a convective Kelvin-Helmholtz instability, while from the trailing edge the separated flow rolls-up and generates a large vortex which has a blocking effect on the leading edge structures. Behind the aerofoil a large wake is formed, mainly due to flow separation at the trailing edge of the aerofoil, and with a smaller contribution from the shear layer formed at the leading edge. The different contributions of these two regions are responsible for the lack of symmetry in the wake, and this is also evident when considering the spectra of the time autocorrelation of the velocity in the shear layer by the leading edge and near the trailing edge. Both the spectra show a peak corresponding to the principal wake shedding frequency, while only the former spectrum shows a smooth peak at higher frequency, corresponding to the vortex generation due to the leading edge Kelvin-Helmholtz shear layer instability. Also, a low frequency peak is present in the former, at approximately half the shedding frequency, corresponding to the flapping motion of the shear layer.

In the ramp-up case, the lift force initially increases monotonically in time even after having attained the maximum incidence angle. Subsequently, it drops dramatically eventually converging to the static stall figure. During the linear growth of the angle of incidence, the separation point moves from the trailing edge towards the leading edge. The backward displacement of the separation line is associated with the formation of a large scale vortex on the suction side of the aerofoil. The unsteady evolution of this vortex, usually termed as dynamic stall vortex, is ultimately responsible for the lift behaviour. As the separation line moves upstream along the suction side, vortices generate, merge, and eventually coalesce into one large dynamic stall vortex. This mechanism is driven by a Kelvin-Helmholtz instability generated at the leading edge. Indeed the convective KH instability associated with the leading edge generated shear layer and continuously produces fine grain vorticity that periodically merges promoting the generation of spanwise oriented large scale structures.

ACKNOWLEDGMENTS

This work was partially supported by the European Commission 7th framework project Pelskin.

[1] R. L. Halfman, H. C. Johnson, and S. M. Haley, "Evaluation of high-angle-of-attack aerodynamic-derivative data and stall-flutter prediction techniques," Technical Report, DTIC Document, 1951.
[2] W. J. McCroskey, "The phenomenon of dynamic stall," Technical Report, DTIC Document, 1981.
[3] W. J. McCroskey, "Unsteady airfoils," Annu. Rev. Fluid Mech. **14**(1), 285–311 (1982).
[4] K. Mulleners and M. Raffel, "The onset of dynamic stall revisited," Exp. Fluids **52**(3), 779–793 (2012).
[5] K. Mulleners and M. Raffel, "Dynamic stall development," Exp. Fluids **54**(2), 1–9 (2013).
[6] C. Brücker and C. Weidner, "Influence of self-adaptive hairy flaps on the stall delay of an airfoil in ramp-up motion," J. Fluids Struct. **47**, 31–40 (2014).
[7] L. E. Ericsson and J. P. Reding, "Fluid dynamics of unsteady separated flow. I. Bodies of revolution," Prog. Aerosp. Sci. **23**(1), 1–84 (1986).
[8] L. E. Ericsson and J. P. Reding, "Fluid dynamics of unsteady separated flow. II. Lifting surfaces," Prog. Aerosp. Sci. **24**(4), 249–356 (1987).
[9] L. E. Ericsson and J. P. Reding, "Fluid mechanics of dynamic stall. I. Unsteady flow concepts," J. Fluids Struct. **2**(1), 1–33 (1988).
[10] L. E. Ericsson and J. P. Reding, "Fluid mechanics of dynamic stall. II. Prediction of full scale characteristics," J. Fluids Struct. **2**(2), 113–143 (1988).
[11] T. Lee and P. Gerontakos, "Investigation of flow over an oscillating airfoil," J. Fluid Mech. **512**, 313–341 (2004).
[12] C. Shih, L. Lourenco, L. Van Dommelen, and A. Krothapalli, "Unsteady flow past an airfoil pitching at a constant rate," AIAA J. **30**(5), 1153–1161 (1992).
[13] M. Acharya and M. H. Metwally, "Unsteady pressure field and vorticity production over a pitching airfoil," AIAA J. **30**(2), 403–411 (1992).
[14] N. L. Sankar and W. Tang, "Numerical solution of unsteady viscous flow past rotor sections," AIAA Paper No. 85-0129, 1985, p. 5.
[15] J. C. Wu, "A study of unsteady turbulent flow past airfoils," Ph.D. thesis, Georgia Institute of Technology, 1988.
[16] I. H. Tuncer, J. C. Wu, and C. M. Wang, "Theoretical and numerical studies of oscillating airfoils," AIAA J. **28**(9), 1615–1624 (1990).
[17] G. N. Barakos and D. Drikakis, "Computational study of unsteady turbulent flows around oscillating and ramping aerofoils," Int. J. Numer. Methods Fluids **42**(2), 163–186 (2003).
[18] S. Wang, D. B. Ingham, L. Ma, M. Pourkashanian, and Z. Tao, "Numerical investigations on dynamic stall of low Reynolds number flow around oscillating airfoils," Comput. Fluids **39**(9), 1529–1541 (2010).

[19] E. Dumlupinar and V. R. Murthy, "Investigation of dynamic stall of airfoils and wings by CFD," in *29th AIAA Applied Aerodynamics Conference* (Curran, 2011), pp. 27–30.
[20] K. Gharali and D. A. Johnson, "Dynamic stall simulation of a pitching airfoil under unsteady freestream velocity," J. Fluids Struct. **42**, 228–244 (2013).
[21] J. A. Ekaterinaris and M. F. Platzer, "Computational prediction of airfoil dynamic stall," Prog. Aerosp. Sci. **33**(11), 759–846 (1998).
[22] M. R. Visbal, "High-fidelity simulation of transitional flows past a plunging airfoil," AIAA J. **47**(11), 2685–2697 (2009).
[23] M. R. Visbal, "Numerical investigation of deep dynamic stall of a plunging airfoil," AIAA J. **49**(10), 2152–2170 (2011).
[24] M. Omidyeganeh and U. Piomelli, "Large-eddy simulation of three-dimensional dunes in a steady, unidirectional flow. I. Turbulence statistics," J. Fluid Mech. **721**, 454–483 (2013).
[25] M. Omidyeganeh and U. Piomelli, "Large-eddy simulation of three-dimensional dunes in a steady, unidirectional flow. II. Flow structures," J. Fluid Mech. **734**, 509–534 (2013).
[26] C. M. Rhie and W. L. Chow, "Numerical study of the turbulent flow past an airfoil with trailing edge separation," AIAA J. **21**(11), 1525–1532 (1983).
[27] J. Kim and P. Moin, "Application of a fractional-step method to incompressible Navier-Stokes equations," J. Comput. Phys. **59**(2), 308–323 (1985).
[28] S. Balay, S. Abhyankar, M. Adams, J. Brown, P. Brune, K. Buschelman, L. Dalcin, V. Eijkhout, W. Gropp, D. Kaushik, M. Knepley, L. C. McInnes, K. Rupp, B. Smith, S. Zampini, and H. Zhang, PETSc Web page, http://www.mcs.anl.gov/petsc, 2015.
[29] V. E. Henson and U. M. Yang, "Boomeramg: A parallel algebraic multigrid solver and preconditioner," Appl. Numer. Math. **41**(1), 155–177 (2002).
[30] M. Omidyeganeh and U. Piomelli, "Large-eddy simulation of two-dimensional dunes in a steady, unidirectional flow," J. Turbul. **12**, N42 (2011).
[31] J. L. Hess and A. M. O. Smith, "Calculation of potential flow about arbitrary bodies," Prog. Aerosp. Sci. **8**, 1–138 (1967).
[32] J. G. Wong, A. Mohebbian, J. Kriegseis, and D. E. Rival, "Rapid flow separation for transient inflow conditions versus accelerating bodies: An investigation into their equivalency," J. Fluids Struct. **40**, 257–268 (2013).
[33] See http://www.pointwise.com/ POINTWISE Web page.
[34] O. Lehmkuhl, A. Baez, I. Rodríguez, and C. D. Perez-Segarra, "Direct numerical simulation and large-eddy simulations of the turbulent flow around a NACA-0012 airfoil," in *7th International Conference on Computational Heat and Mass Transfer* (Begell House, 2011), pp. 1–8.
[35] I. Rodríguez, O. Lehmkuhl, R. Borrell, and A. Oliva, "Direct numerical simulation of a NACA0012 in full stall," Int. J. Heat Fluid Flow **43**, 194–203 (2013).
[36] A. Skillen, A. Revell, A. Pinelli, U. Piomelli, and J. Favier, "Flow over a wing with leading-edge undulations," AIAA J. **53**(2), 464–472 (2014).
[37] C. W. Knisely, "Strouhal numbers of rectangular cylinders at incidence: A review and new data," J. Fluids Struct. **4**(4), 371–393 (1990).
[38] M. Kiya and K. Sasaki, "Structure of a turbulent separation bubble," J. Fluid Mech. **137**, 83–113 (1983).
[39] N. J. Cherry, R. Hillier, and M. E. M. P. Latour, "The unsteady structure of two-dimensional separated-and-reattaching flows," J. Wind Eng. Ind. Aerodyn. **11**(1), 95–105 (1983).
[40] I. P. Castro and A. Haque, "The structure of a turbulent shear layer bounding a separation region," J. Fluid Mech. **179**, 439–468 (1987).
[41] L. M. Hudy, A. M. Naguib, and W. M. Humphreys, Jr., "Wall-pressure-array measurements beneath a separating/reattaching flow region," Phys. Fluids (1994-present) **15**(3), 706–717 (2003).
[42] J. C. R. Hunt, A. A. Wray, and P. Moin, "Eddies, stream, and convergence zones in turbulent flows," Center for Turbulence Research Report CTR-S88, 1988, pp. 193–208.
[43] S. Burgmann, J. Dannemann, and W. Schröder, "Time-resolved and volumetric PIV measurements of a transitional separation bubble on an SD7003 airfoil," Exp. Fluids **44**(4), 609–622 (2008).
[44] S. Burgmann and W. Schröder, "Investigation of the vortex induced unsteadiness of a separation bubble via time-resolved and scanning PIV measurements," Exp. Fluids **45**(4), 675–691 (2008).
[45] Z. Yang and P. R. Voke, "Large-eddy simulation of boundary-layer separation and transition at a change of surface curvature," J. Fluid Mech. **439**, 305–333 (2001).
[46] P. R. Spalart and M. K. Strelets, "Mechanisms of transition and heat transfer in a separation bubble," J. Fluid Mech. **403**, 329–349 (2000).
[47] I. E. Abdalla and Z. Yang, "Numerical study of the instability mechanism in transitional separating–reattaching flow," Int. J. Heat Fluid Flow **25**(4), 593–605 (2004).
[48] M. Breuer and N. Jovicic, "Separated flow around a flat plate at high incidence: An LES investigation," J. Turbul. **2**(1), N18 (2001).
[49] M. Breuer and N. Jovicic, "An LES investigation of the separated flow past an airfoil at high angle of attack," in *Direct and Large-Eddy Simulation IV* (Springer, 2001), pp. 165–172.
[50] G. Haller, "Distinguished material surfaces and coherent structures in three-dimensional fluid flows," Phys. D **149**(4), 248–277 (2001).
[51] S. C. Shadden, F. Lekien, and J. E. Marsden, "Definition and properties of Lagrangian coherent structures from finite-time Lyapunov exponents in two-dimensional aperiodic flows," Phys. D **212**(3), 271–304 (2005).
[52] G. Haller, "Lagrangian structures and the rate of strain in a partition of two-dimensional turbulence," Phys. Fluids (1994-present) **13**(11), 3365–3385 (2001).
[53] S. Kida and H. Miura, "Identification and analysis of vortical structures," Eur. J. Mech.-B/Fluids **17**(4), 471–488 (1998).